Dirac cone shift of a passivated topological Bi_{2}Se_{3} interface state

Gregory S. Jenkins, Don C. Schmadel, Andrei B. Sushkov, H. Dennis Drew, Max Bichler, Gregor Koblmueller, Matthew Brahlek, Namrata Bansal, and Seongshik Oh

Phys. Rev. B **87**, 155126 — Published 15 April 2013

DOI: 10.1103/PhysRevB.87.155126

Dirac cone shift of a passivated topological Bi_2Se_3 interface state

Gregory S. Jenkins* and Don C. Schmadel
Department of Physics, University of Maryland at College park, College Park, Maryland, 20742, USA and
Center for Nanophysics and Advanced Materials,
University of Maryland at College park, College Park, Maryland, 20742, USA

Andrei B. Sushkov and H. Dennis Drew
Department of Physics, University of Maryland at College park, College Park, Maryland, 20742, USA
Center for Nanophysics and Advanced Materials,
University of Maryland at College park, College Park, Maryland, 20742, USA and
Materials Research Science and Engineering Center,
University of Maryland at College park, College Park, Maryland, 20742, USA

Max Bichler and Gregor Koblmueller
Walter Schottky Institut and Physik Department,
Technische Universitat Munchen, D-85748 Garching, Germany

Matthew Brahlek, Namrata Bansal, and Seongshik Oh
Department of Physics and Astronomy, The State University of New Jersey, Piscataway, New Jersey 08854, USA

Gated terahertz cyclotron resonance measurements on epitaxial Bi_2Se_3 thin films capped with In_2Se_3 enable the first spectroscopic characterization of a single topological interface state from the vicinity of the Dirac point to above the conduction band edge. A precipitous drop in the scattering rate with Fermi energy is observed that is interpreted as the surface state decoupling from bulk states and evidence of a shift of the Dirac point towards mid-gap. Near the Dirac point, potential fluctuations of 50 meV are deduced from an observed loss of differential optical spectral weight near the Dirac point. Potential fluctuations are reduced by a factor of two at higher surface Fermi levels in the vicinity of the conduction band edge inferred from the width of the scattering rate step. The passivated topological interface state attains a high mobility of 3500 $cm^2/V{\cdot}s$ near the Dirac point.

I. INTRODUCTION

The topological insulator (TI) is a unique new state of matter that is a bulk insulator possessing a topologically protected metallic surface state of massless particles known as Dirac fermions. Key properties of this surface state are spin-momentum locking, suppression of back scattering, and an intrinsic magneto-electric effect.[1,2] The experimental realization of this state of matter has sparked great interest owing not only to their potential use in spintronics and quantum computing but in the investigation of the fundamental nature of topologically nontrivial quantum matter.[3,4]

The surface state Dirac point of most currently known TIs lies below the top of the bulk valence band (like Bi_2Te_3).[1,2] This deficiency is particularly problematic since many interesting phenomena are predicted to occur at or near the Dirac point, like the 1/2-quantized Hall step.[1,2] In this regard, Bi_2Se_3 is one of the few attractive materials since its single Dirac point lies well above the valence band.[5] However, Bi_2Se_3 is especially prone to defect doping in the bulk which dominates the conduction.[6–9] Surface doping from defects and atmospheric exposure not only lower the mobility but result in accumulated surfaces that inhibit conventional gating techniques from decoupling the surface states from bulk states.[9–12]

Passivating and controlling the electronic properties of the TI surface state involves interfacing with other materials. The proximity of the topological insulator to trivial insulators, magnetic materials, and superconductors are either expected to induce changes in the Dirac cone[13,14] or fundamentally change the nature of the interface state giving rise to exciting new emergent phenomena.[1–4] The usual surface sensitive techniques that have successfully characterized the vacuum interface are not useful when the topological interface state is deeply buried beneath other materials.[1,2,15,16] The interpretation of dc transport measurements of the TI surface state is confounded by the multiple conductivity channels generally expected in TIs: a bulk contribution with two inequivalent surfaces, each with a topological surface state and bulk screening surface layer (depicted in Figure 1(a)). To characterize these systems, new experimental techniques are required.

In this article, all of the above issues are experimentally addressed. A thin film of Bi_2Se_3 is capped with the trivial insulator In_2Se_3 that protects the Bi_2Se_3 from atmospheric degradation and dopes the surface enabling the Dirac point to be reached by conventional gating while achieving high mobilities.[17,18] Evidence of a large shift of the Dirac point towards the conduction band edge relative to the vacuum interface is reported for the first time demonstrating the possibility of controlling the Dirac cone in other TI systems. The first experimental determination of the surface state scattering rate as a

function of Fermi energy provides a detailed map of the interplay between the bulk and TI surface state carriers. The energy scale of potential fluctuations characterized near the Dirac point agrees with other measurement techniques,[16,19] and is reduced by a factor of two near the conduction band edge.

II. METHODS

Measurements from three gate-modulated terahertz transmission techniques are presented: broadband FTIR measurements, cyclotron resonance, and the complex Faraday angle. The gate-modulated terahertz cyclotron resonance data set performed at our lowest measured frequency of $\omega/2\pi = 0.74$ THz will be discussed in the most detail since the topological surface state transport properties are most easily related to features in the raw data set. In the cyclotron resonance measurements, each conduction channel in the film is a distinct Lorentzian response distinguishable by the sign of the charge, cyclotron mass m_c, spectral weight ne^2/m_c, and carrier scattering rate γ. Spatial location of the carrier contributions in the film are ascertained by concurrently modulating a semi-transparent top gate that spatially modulates the charge distribution in the film in a predictable way.

Device Description

The device is depicted in Figure 1(b). A Bi_2Se_3 60 quintuple layer film is grown epitaxially onto a 0.5 mm thick sapphire substrate of area 1x1 cm square.[17] A 10 nm thick In_2Se_3 capping layer is immediately deposited without breaking vacuum. The In_2Se_3 layer is verified to be crystalline α-phase via RHEED measurements as described in reference 18.

Two contacts are made to the film using silver epoxy. Parylene-C is deposited to a thickness of 590 nm, conformally encasing the sample on both the top and bottom surfaces with a measured thickness uniformity better than 10 nm. NiCr films are evaporated onto the Parylene-C, the bottom surface serving as an absorptive broadband antireflection coating and the top surface as a gate patterned by shadow masking. The antireflection coating is deposited to a sheet resistance of 275 $\Omega/\Box$ and the gate to 400 $\Omega/\Box$. Two contacts to the gate are made using the same silver epoxy.

Parylene-C optical properties are characterized utilizing FTIR transmission measurements. The static dielectric constant is measured with a capacitance bridge and found to be 2.8 at low temperature consistent with other measurements.[20] The gate provides 2.6×10^{10} e/cm^2 per volt. Breakdown voltages as large as 200 V is achieved.

Optical Methods Overview

In order to gain insight into the utility of both zero-gate and gate-modulated terahertz transmission measurements, approximate optical formulas are presented which emphasize the physical concepts. In this section, the transmission of a single thin-film of Bi_2Se_3 on a dielectric substrate is considered. The gate-modulated and zero-gate transmission is simply related to the multiple conductivity channels present in the film with their associated Drude parameters. Additional transmission effects associated with the gate, antireflection coating, and phonons are included in the full optical model used in the analysis described in Appendix A.

The normal-incident transmission T of a thin film (on a dielectric substrate) with multiple contributions to the conductivity σ relative to the transmission of the bare substrate T_0 is given by $\frac{T}{T_0} = |\frac{n_{sub}+1}{n_{sub}+1+\sum y_i}|^2$ where $y_i = Z_0\sigma_i$ is the surface admittance, n_{sub} is the index of refraction of the substrate, and Z_0 is the impedance of free space. In a magnetic field, each Drude conductivity component may be written in the circular polarization basis as $\sigma^{\pm} = \frac{\omega_{ps}/Z_0}{\gamma - \imath(\omega \pm \omega_c)}$ where $\omega_c = eB/c\,m_c$ is the cyclotron frequency, m_c is the cyclotron mass, $\omega_{ps} = Z_0 ne^2/m$ is the two dimensional plasma frequency, $\gamma = 1/\tau$ is the inverse transport lifetime (scattering rate), ω is the radiation frequency, n is the two dimensional carrier density, and e is the electronic charge.

Cyclotron resonance (CR) transmission measurements are performed at fixed frequency with normally incident circularly polarized light as a function of applied magnetic field. A resonant Lorentzian-like absorption occurs in the CR transmission when the B-field is at a particular value B_{res} defined when $\omega = \omega_c$, or $B_{res} = (c\omega/e)m_c$. The polarity and value of the B-field resonance determines the sign and mass of the carriers. In the limiting case $y_i << n_{sub} + 1$, the gate-modulated transmission reduces to

$$\Delta T^{\pm} = -\frac{2T_0}{n_{sub}+1} Re(\sum Z_0\, \Delta\sigma_i^{\pm}) \qquad (1)$$

This is defined as the differential cyclotron resonance (Δ-CR) and can be thought of as a sum of differences of Lorentzians.

Similar to the cyclotron resonance measurements, the complex Faraday angle is measured at normal incidence and a fixed frequency as a function of magnetic field. The technique, detailed elsewhere,[21] involves modulating the incident polarization allowing simultaneous measurement of the circular dichroism ($Im(\theta_F)$) that is related to the absorptive part of the conductivity similar to cyclotron resonance as well as the Faraday rotation angle ($Re(\theta_F)$) that is related to the reactive part of the conductivity. When the scattering rate is much less than the cyclotron frequency, $Im(\theta_F)$ ($Re(\theta_F)$) shows a simple Lorentzian resonance (antiresonance) centered at B_{res}.[21] Contrary to CR measurements, n and p-type carrier resonances

will simultaneously appear in both polarities of magnetic field but with opposite sign.

Fourier transform spectroscopy (FTIR) transmission measurements are performed in zero magnetic field ($\omega_c = 0$) with unpolarized incident light.

A far-infrared molecular laser pumped by a CO_2 laser provides the fixed frequency source for the Faraday angle and cyclotron resonance measurements.[21] Circular polarized light for the cyclotron resonance measurement is generated using quartz quarter-waveplates with NiCr antireflection coatings. A GaAs 2-DEG heterostructure is used to set the waveplate angle, verify the retardance of the waveplates, and serves to calibrate the Faraday angle measurements and the sign of the charge carriers in the cyclotron resonance measurements.[21]

III. OPTICAL RESULTS

Zero-gate data

Zero-gate normally incident transmission measurements are reported in Figures 1(c) and (d) for the device schematically represented in Figure 1(b). The zero-gate cyclotron resonance transmission measurement is shown in the inset of Figure 1(c). The minimum transmission (maximum absorption) occurs at a positive magnetic field indicating dominant n-type carriers of mass $m_c \approx 0.19\ m_0$. The Fourier transform spectroscopic transmission measurement is reported in Figure 1(c) and the complex Faraday angle θ_F in Figure 1(d). Fits to these data using a single-fluid Drude model for the conductivity, depicted by the blue curves, reveal a large carrier density $n \gtrsim 10^{13}$ cm^{-2} and a dominant cyclotron mass that is much larger than the conduction band edge mass $m_c = 0.15\ m_0$ measured in bulk single crystals.[6,7,22–24] Deviations between the θ_F data and fit are outside of measurement error, hinting at small contributions from other conducting channels.

DC transport measurements on similarly grown films, performed over a wide range of thicknesses, characterize the bulk conductivity that is small compared to surface contributions.[10] The bulk carrier density is measured to be $\lesssim 5 \times 10^{17}$ cm^{-3},[10] and corresponds to a bulk Fermi level of $\lesssim 11$ meV above the conduction band edge. This measured bulk density for a 60 nm thick film is a small fraction of the zero-gate optically measured carrier density. Therefore, the large majority of carriers measured at zero-gate reside in a top and/or bottom surface accumulation layer that include topological surface states.

Gate-modulated Data

Modulating the top gate voltage at ~ 1 Hz and measuring the differential cyclotron resonance (Δ-CR) reveals the top topological interface state properties. The data

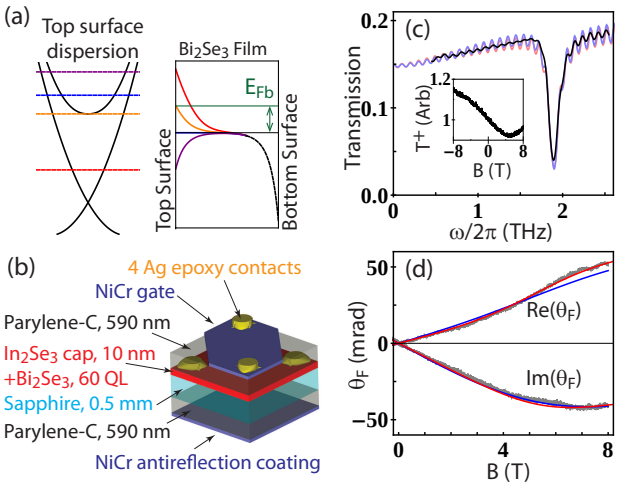

FIG. 1: **Zero-gate normal incident transmission measurements** (a) A band bending schematic showing the conduction band edge (CBE) relative to the bulk chemical potential (green), and the corresponding Dirac cone Fermi level associated with the vacuum interface, when a variable gate voltage is applied to the top surface. Purple through red correspond to increasingly negative gate voltages. The bottom surface (black) is accumulated due to defects. (b) A schematic represents the measured device. (c) Fourier transform (FTIR) transmission spectrum (black) is measured at 6 K. A single-fluid Drude model fit (blue) gives $\gamma = 1/\tau = 7.3$ THz and $\omega_{ps}/(2\pi) = 27.9$ THz that translates to a carrier density $n = 1.23 \times 10^{13}$ cm^{-2} for a mass of $m = 0.21$. Oscillations in the FTIR data are due to Fabry-Perot etalon in the sapphire substrate. (inset) Measured 10 K cyclotron resonance transmission at $\omega/(2\pi)$=0.74 THz. (d) Complex Faraday angle measured at 10 K and $\omega/(2\pi)$=0.74 THz (black). A single-fluid Drude model fit (blue) gives $\gamma = 1/\tau = 7.4$ THz, $n = 1.1 \times 10^{13}$ cm^{-2}, and $m_c = 0.21$. The red curves in figures (c) and (d) are computed from a three-fluid Drude model with parameters reported in Figure 3.

is presented in Figure 2(a) where each curve is the difference of the measured CR resonance at two gate voltages, $V_g \pm \Delta V/2$ where $\Delta V = 50$ V and V_g is the average gate voltage. Each curve is associated with a different average gate voltage, color-coded by the legend at the top of the figure.

The largest negative average gate voltage in Figure 2(a) shows a resonant component at $B \approx 2$ T, corresponding to a cyclotron mass much less than the bulk mass.[6,7,22] Since the cyclotron mass $m_c = \hbar k_F / v_F$ is expected to go to zero as the Dirac point is approached, such a small measured cyclotron mass is direct evidence of the topological interface state. Utilizing the ARPES measured dispersion of the TI surface state provided in Appendix A, the corresponding Fermi level is approximately 45 meV above the Dirac point, far below the conduction band edge of 190 meV observed on Bi_2Se_3.[25,26] Even though a more sophisticated analysis of the scattering rate will be given later, an estimate for the feature

at 2 T taken directly from the raw data is given by the full width at half maximum, $\Delta B/B_{res} = 2\gamma/\omega \approx 4$, so the inverse lifetime $\gamma = 1/\tau$ is in the vicinity of 9 THz.

The gate-modulated complex Faraday angle data is reported in Figures 2(b) and (c) since it provides additional information being sensitive to not only the absorptive part of the conductivity (as is the case for the Δ-CR measurements), but the reactive part as well.[21]

Such a small measured mass associated with the top surface indicates that the majority of the carriers measured at zero-gate are associated with the bottom surface. As depicted in Figure 1(a) for a surface Fermi level near the Dirac point (red), a depletion region necessarily exists in the bulk. As the gate increases, the surface state and depletion region begin filling (orange), eventually leading to a bulk accumulated layer (purple). For a bulk Fermi level of 11 meV above the conduction band edge, gating from the Dirac point to the flat band condition (orange) requires transferring 4.4×10^{12} cm^{-2} carriers into the TI surface state Dirac cone. When the surface Fermi level is at the Dirac point, the topological surface state is empty so does not contribute to screening effects. In this case, the usual Thomas-Fermi screening of the applied electric field by a dilute metal or doped semiconductor produces a depletion length of $W = \sqrt{2\epsilon\Delta E/en}$,[27] where ΔE is the energy of the conduction band edge at the surface relative to flat band. The number of carriers required to fill this depletion region is $nW = 2.7\times10^{12}$ cm^{-2}. Therefore, the required number of carriers to move if gating from the Dirac point to flat band is $\approx 7 \times 10^{12}$ cm^{-2}. This is substantially more than the net number of carriers the gate can transfer when gating from 0 V to −170 V, a voltage that drives the surface Fermi level to very near the Dirac point. Assuming the ARPES characterized Dirac spectrum for the topological surface state, this means that at zero gate voltage, the bulk carriers near the top surface must be slightly depleted, and only $\approx 2 \times 10^{12}$ cm^{-2} excess carriers exist on the top surface. The majority of the $\sim 10^{13}$ cm^{-2} carriers measured at zero gate therefore must be associated with an accumulated bottom surface.

However, two distinct large spectral weight contributions with different masses associated with the bottom surface topological surface state and bottom surface bulk accumulation region are not clearly discernible in the broad zero-gate responses reported in Figure 1(c) and (d). The differential optical measurements are insensitive to carrier contributions that are not significantly modulated by the top gate and are therefore expected to be very insensitive to the bottom surface properties.

IV. ANALYSIS AND DISCUSSION OF THE DATA

The picture that emerges is the one depicted in Figure 1(a). An accumulated bottom surface dominates the zero-gate measurements. The gate modulates two top surface carrier contributions, one associated with the top topological surface state (TSS) and the other with a modulated top bulk (MTB) screening region.

Gate-modulated two-fluid Drude model

The full electro-static (Thomas-Fermi) screening solution for a topological insulator in the presence of an externally applied electric field is derived in Appendix A. The net charge transferred from the gate to the TI film is divided between the topological surface state (TSS) and the rest of the bulk (MTB). The proportions when gating away from the Dirac point are plotted in Figure 3(a) as a function of gate voltage. Since the carrier density in the ARPES measured Dirac cone is known as a function of gate voltage, the Fermi level and cyclotron mass $m_c = \hbar k_F/v_F$ as a function of gate voltage can be calculated from the dispersion and are shown in Figures 3(b) and (c). Figure 3(c) shows that the Dirac point is indeed located in the vicinity of −170 V given that $m_c = 0.08$ at average gate voltage −150 V, as was stated previously without full justification.

To gain further insight into the various structures in the Δ-CR data set and their evolution as a function of average gate voltage, a two-fluid Drude conductivity is incorporated into the differential transmission model. The two modulated carrier contributions physically correspond to the TSS and MTB carriers. The carrier densities and TSS cyclotron mass are constrained as derived in Figures 3(a) and (c). The only remaining gate-dependent free parameters are the scattering rates of the two carrier contributions and the cyclotron mass of the MTB carriers.

The modulated transmission is very insensitive to the precise Drude parameters of the unmodulated bottom surface accumulation layer (BSAL), but its non-negligible contribution to the surface admittance needs to be included in the optical model. Since the zero-gate measurements are very sensitive to the this dominant conductivity contribution, concurrent simulation of the zero-gate measurements and the differential measurements that include all three carrier contributions (TSS, MTB, and BSAL) allow fine tuning of the bottom surface parameters. Ultimately, it is found that the BSAL conductivity found in this manner compared with that attained solely from fitting zero-gate measurements does not appreciably affect the differential transmission model.

Figures 2(d-f) show the modeled differential optical signals, and Figures 1(c) and (d) (red curves) show the modeled zero-gate signals. Comparisons with other Δ-CR measurements at higher frequencies as well as gated FTIR spectroscopy data are shown in Figure 6.

For surface Fermi levels below the conduction band edge, a constant scattering rate and cyclotron mass for the MTB carriers best fit the differential data. For this especially important range, the only remaining variable gate-dependent free parameter is the scattering rate of the TI interface state. Figures 3(a), (c), and (e) summa-

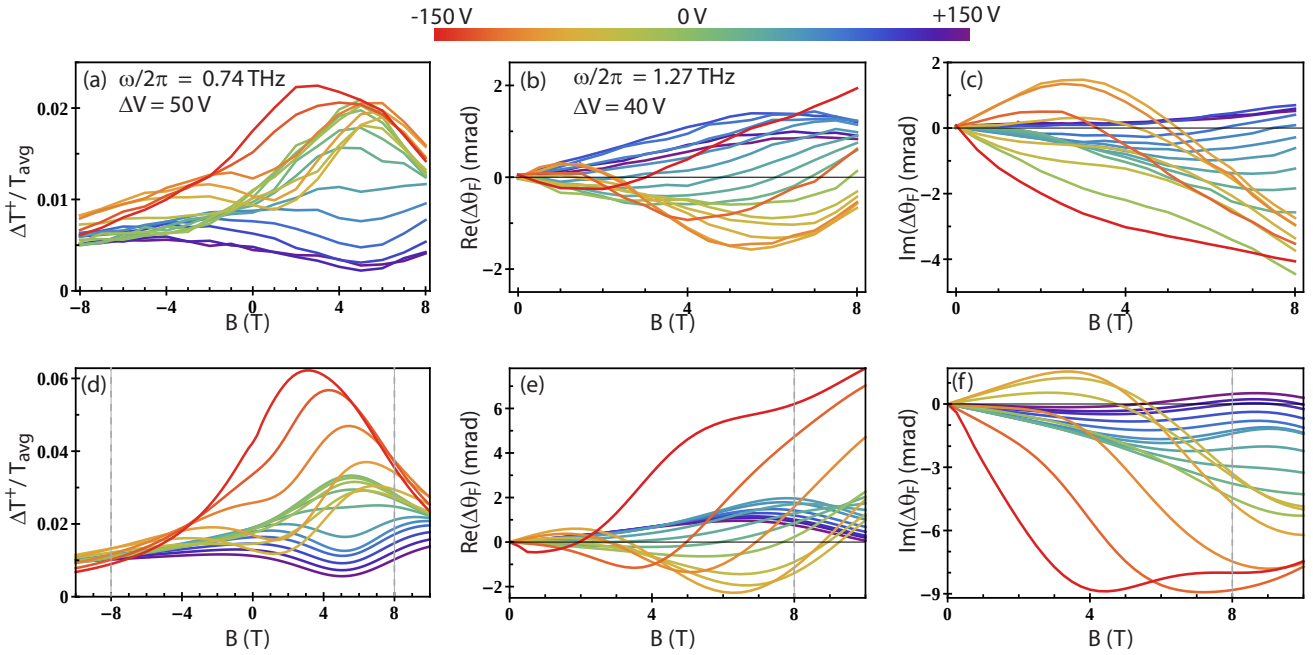

FIG. 2: **Gated measurements at 10K:** All optical signals are differences between two gate values, $V_g \pm \Delta V/2$. Average gate values V_g for each plot are coded according to the colored bar at the top of the figure. Shown on each data graph is the radiation frequency $\omega/(2\pi)$ and ΔV value. (a) Differential cyclotron resonance data normalized to the average with a standard deviation of the mean of 5×10^{-4} measured at every integer B-field. (b,c) Differential Faraday angle data measured at every 1/2-integer B-field with a standard deviation of the mean of 30 μrad (d-f) The modeled optical responses correspond to the same V_g and ΔV values appearing in the respective data sets (a-c).

rize the Drude parameters which most closely reproduce the data sets, and the constant BSAL parameters are included in the caption.

All the features of the data are reproduced over a wide range of applied voltages, magnetic fields, and frequencies, but interesting deviations appear at high negative gate voltages in all data sets where the top TI surface state carrier density is small. The one central assumption in the optical models is that the topological surface state carrier density and cyclotron mass are described by the ARPES measured Dirac cone dispersion when gating away from the Dirac point. Deviations between the model and the data therefore highlight important differences between the topological interface state that exists at the In_2Se_3/Bi_2Se_3 interface and the vacuum interface characterized by ARPES.

Before analyzing these deviations, it is instructive to consider the relationship between the modeled optical signals of Figure 2(d) and the two-fluid Drude parameters that best fit the data summarized in Figure 3. All the features appearing in the raw data set of Figure 2(a) can then be directly understood in terms of the individual conductivity components and their associated Drude parameters.

Intuitive description of the Δ-CR model

The modeled optical signals in relation to the Drude parameters can be qualitatively understood most easily by considering the Δ-CR model curves of Figure 2(d). As discussed previously, a cyclotron resonance is a Lorentzian-like absorption where n/m_c defines the weight, γ defines the width, and m_c defines the center of the resonance via $B_{res} = (c\,\omega/e)m_c$. When a gate voltage is applied, these parameters can change. As encapsulated by Equation 1, a single Δ-CR curve in Figure 2(d) is the sum of differences between two pairs of Lorentzians, a pair for the TSS and MTB contributions.

Near zero gate voltage, the mass and scattering rate of the TSS and MTB carriers do not change much with gate voltage as shown in Figure 3. Only the weights of the resonances change. Since $\gamma_{TSS} >> \gamma_{MTB}$ and the change in carrier density $\Delta n_{TSS} \sim \Delta n_{MTB}$, the resulting line shape appears Lorentzian centered on the mass of the MTB contribution corresponding to a resonant B-field of $\sim$ 5.2 T. As the gate is increased and the surface Fermi level moves higher, the dominant response is the MTB contribution that has a growing scattering rate and carrier density. Taking the difference between two Lorentzians that have slightly different widths (γ) will cause a suppression of the peak at the resonant B-field. A slight simultaneous increase in mass shifts one of the resonances in B-field relative to the other causing a slight

skew in the difference curve. In this case, the part of the differential cyclotron resonance occurring at low B-fields are slightly more suppressed than the higher fields due to the changing MTB mass. The gradual increase of the large TSS scattering rate causes a suppression of the resonant peak over a broad range of B-field.

As one gates from zero to negative gate voltages toward the Dirac point, the only MTB Drude parameter that changes is the carrier density. Therefore, the Δ-CR of the MTB carriers maintain an approximately constant Lorentzian−like line shape.

The modulated top bulk (MTB) region described as one Drude term is conceptually appealing considering its physical interpretation. Gating from the Dirac point to flat band only fills the depleted bulk with carriers, providing an explanation as to why the MTB scattering rate and mass are gate independent over this range. As the carriers begin to accumulate at positive gate voltages, some of the bulk states gradually become confined states at the top surface increasing the bulk/surface scattering channels while also increasing bulk scattering from surface defects. The mass of the accumulated carriers also gradually increases, heading toward the bigger mass found on the more highly accumulated bottom surface (see Appendix C regarding the large measured bulk cyclotron masses).

At all negative gate voltages, the TSS response is superimposed on a constant Lorentzian MTB background. The mass and number density decrease with surface Fermi level consistent with the ARPES measured Dirac dispersion as the Dirac point is approached. The shifting of the peak locations to lower magnetic field are a direct result of the decreasing cyclotron mass of the TI surface state.

The very rapid change of the TSS scattering rate occurring at approximately −70 V gives rise to the peak-dip-hump structure. The depth of these modulations in the Δ-CR curves of Figure 2(d) are extremely sensitive to the rate of change of the scattering rate, and therefore extremely sensitive to the shape of the scatterring rate curve shown in Figure 3(d).

To emphasize this point, model results using a constant TSS scattering rate are shown in Figure 4 where all other model parameters are exactly the same as reported in Figure 3. In this case, the TSS contribution to Δ-CR are a series of skewed Lorentzian-like peaks whose weight increases with decreasing surface Fermi level, and whose resonant location ($B_{res} \sim m_c$) decrease towards zero B-field as expected from a Dirac cone dispersion. The peak-dip-hump structure that is present in the data in Figure 2(d) is conspicuously missing in Figure 4.

The modeled Δ-CR peaks for the TSS contribution at the highest negative gate voltages can be thought of as just the CR peak of the higher surface Fermi level since very little relative spectral weight exists in the lower surface Fermi level peak. This is most vividly illustrated by considering the hypothetical scenario where the lowest surface Fermi level is actually at the Dirac point where

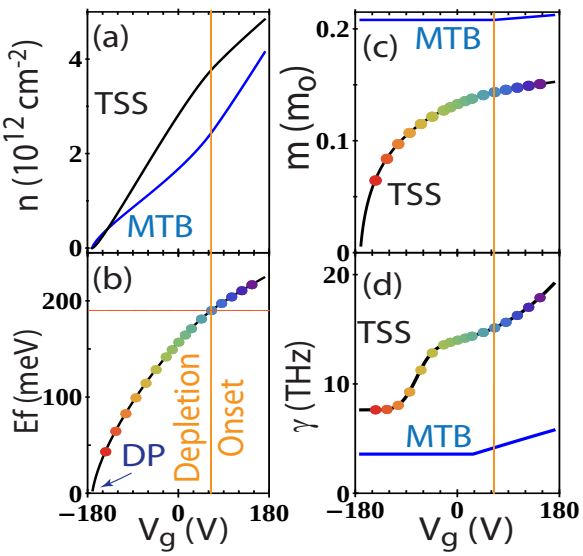

FIG. 3: **Model parameters:** Three n-type Drude terms model the reported differential optical measurements. The BSAL parameters are $n = 1.0 \times 10^{13}$ cm^{-2}, $m_c = 0.25\ m_0$, and $\gamma = 1/\tau = 9.4$ THz. The red through purple dots on all graphs depict the same average voltages applied as in Figure 2(a). The solid orange lines depict the depletion onset and the red dashed lines depict the conduction band edge (CBE), inferred from the ARPES measured dispersion.(a) The fraction of charge moved by the gate in the MTB (blue) carrier contribution and the TSS (black), where the flat-band bulk density is 5×10^{17} cm^{-3}, shown as a function of V_g. (b) The TSS Fermi level with respect to the Dirac point. (c) The cyclotron mass in units of the bare electron mass m_0 and (d) the scattering rates (inverse lifetimes) are shown for the MTB (blue) and TSS (black) carrier contributions.

there are no carriers. The difference curve then would be exactly the TSS CR curve at the higher surface Fermi level, superimposed on the MTB contribution.

An understanding of all the Δ-CR curves can be summarized. The MTB contribution is the dominant response at positive gate voltages. At negative voltages, the MTB contribution to Δ-CR is roughly constant since only n is changing. The peak-dip-hump structure that develops is associated with the TSS contribution primarily due to the rapidly changing scattering rate. The shifting of this peak-dip-hump structure with B-field is a result of the rapidly changing mass expected from a Dirac cone. At the highest negative gate voltages, a single TSS cyclotron resonance is superimposed on a constant Δ-CR MTB Lorentzian-like peak.

Comparison of model and data

Deviations in magnitude between the model and data for $V_g \lesssim -100$ V become progressively larger as the Dirac point is approached, indicating that the presumed

ARPES Dirac cone overestimates the Δ-CR spectral weight of the TI interface state. The Δ-CR signals are proportional to changes in the optical spectral weight, $\Omega = ne^2/m_c$. The ideal Dirac cone dispersion predicts $\Omega \propto k_F v_F \propto \sqrt{n}$ which goes to zero at the Dirac point as do both n and m_c. The differential spectral weight $d\Omega/dn \sim 1/\sqrt{n}$ tends to rapidly increase as the Dirac point is approached as demonstrated by the model in Figure 2(d).

However, potential fluctuations are not included in the Dirac cone model. In the presence of potential fluctuations,[16,19,28,29] the spectral weight saturates to some non-zero rms value as the Dirac point is approached. This saturation of the spectral weight reduces the observed differential spectral weight below that predicted by a Dirac cone dispersion.

Within this interpretation, these deviations provide a means to estimate the characteristic potential fluctuation energy. The first significant deviation between model and data of Figures 2(a) and (d) begins with average voltage $V_g = -105$ V with its associated lowest voltage of -130 V. From Figure 3(b), the corresponding TSS Fermi level is ~ 60 meV above the Dirac point. This estimate of the potential fluctuations agrees well with other estimates.[19]

The model tracks the peak and peak-dip-hump structure of the data as the gate is increased from the vicinity of the Dirac point. The shifting of these structures to higher B-fields in the model is a result of the increasing cyclotron mass of the topological surface state. The agreement of the B-field location of these structures with the data therefore means the ARPES measured Dirac cone dispersion well describes the cyclotron mass of the carriers.

The peak-dip-hump structure of the Δ-CR model in Figure 2(d) at negative gate voltages are caused by the rapidly increasing TI interface state scattering rate with surface Fermi energy occurring in the vicinity of -70 V. The model is extremely sensitive to the functional form of the TSS scattering rate allowing accurate determination of this parameter by comparing to the data. The overall shifting of the structure to higher B-field observed in the data as the gate is increased ensures that the rapidly changing scattering rate is associated with the increasing mass of the topological surface state.

Step in TI surface state scattering rate

The most interesting feature in the scattering rate of Figure 3(e) is a large step that occurs at -70 V, well below the inferred gate voltage of the conduction band edge that is 190 meV above the Dirac point as measured by ARPES. This behavior is very different from that observed in graphene.[28,30] The step in scattering rate may relate to the decoupling of the topological surface state from bulk scattering channels. This is expected to occur at the onset of depletion when the surface and bulk states at the interface become non-degenerate and the scattering channel of the topological surface carriers into the bulk is eliminated. In this interpretation, the step in scattering rate is the optical signature of the conduction band edge. No such signature is present near 190 meV.

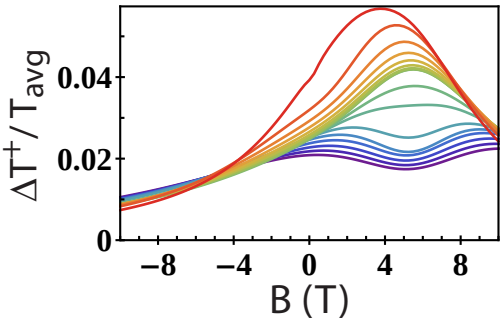

FIG. 4: **Δ-CR model with constant γ_{TSS}** The Δ-CR model is the same as in Figure 2(d) with exactly the same parameters, but the top topological surface state scattering rate is set to a constant 9.4 THz.

The consequence is that the Dirac point for the In_2Se_3/Bi_2Se_3 interface is much closer to the bulk conduction band than the ARPES characterized vacuum interface. For a shifted Dirac cone where the conduction band edge is at $V_g = -70$ V, the corresponding surface Fermi level is calculated from Thomas-Fermi screening arguments, similar to the results of Figure 3(b). The conduction band edge is ~ 80 meV above the Dirac point (and a refined estimate of the potential fluctuation onset at $V_g = -130$ V is $\sim$50 meV as described in Appendix C). The interface state Dirac point appears shifted by ~ 110 meV relative to the vacuum interface.

Such a shift of the Dirac point is not unexpected for the In_2Se_3/Bi_2Se_3 interface.[13,14] Since the existence of the topological surface state is due to the crossover of a topological insulating bulk-band-inverted semiconductor to a bulk trivial insulator,[2,13] the properties of this interface state should be contingent upon the material properties of both the topological insulator as well as the trivial insulator.

For the ARPES measurements on bulk topological insulating materials, the vacuum takes the part of the topologically trivial insulator. The more general case has been solved within a two band model using $k \cdot p$ perturbation theory in reference 13. This theory shows that the Dirac spectrum is modified as a function of the gap of the trivial insulator and any potential step at the interface. Thus for a trivial insulator with a gap of 1.2 eV in contact with a topological insulator with a bulk gap of 300 meV in the presence of a potential step of 0.5 eV, the Dirac point of the topological surface state shifts by 100 meV. This potential step can result from differences in the work function of the two materials or the presence of a dipole layer at the interface.[31] While not enough is known about the In_2Se_3/Bi_2Se_3 interface to predict the

potential step,[32–34] this calculation demonstrates that a shift of the right magnitude is expected to occur with reasonable values of a potential step.

Within this picture, the location of the step in scattering rate is naturally explained, and the width of the step is a consequence of potential fluctuations. The half-width of the derivative of the scattering rate step with respect to the surface Fermi level gives an estimate of $\sim$ 25 meV for the potential flucutation energy scale at the conduction band edge, which takes into account the shift of the Dirac cone as described in Appendix C. Enhanced screening from a higher density of surface carriers as well as contributions from bulk carriers tend to reduce the potential fluctuations compared to the Dirac point vicinity.[28,35]

V. CONCLUSION

The topologically protected surface state carriers are spectroscopically characterized in a passivated Bi_2Se_3 thin film interfaced with the trivial insulator In_2Se_3. The Dirac cone is observed by tracking the cyclotron mass as a function of surface state carrier density, and the transport scattering rate of the Dirac cone carriers is reported as a continuous function of gate voltage from the vicinity of the Dirac point up through the conduction band edge. The mobility of the topological surface state carriers attains a value of $\sim$ 3500 cm^2/V·s near the Dirac point calculated directly from the transport scattering rate and cyclotron mass. A large step in the topological surface state scattering rate is interpreted as the optical signature of the conduction band edge and represents a Dirac point that is 110 meV closer to the bulk conduction band edge compared with the vacuum interface characterized by ARPES. The Dirac cone carriers are highly scattered, a factor of 2 to 3 larger than the modulated bulk carriers over the entire range of applied gate voltage. The characteristic energy scale of potential fluctuations is 50 meV in the vicinity of the Dirac point and 25 meV at the conduction band edge.

The magneto-optical techniques presented here provide a powerful means to characterize the topological surface state even when it is buried deep beneath other materials. A whole range of possibilities are now open for exploration which were not previously possible using other known surface sensitive probes like ARPES[11,25,36,37] or STM.[16,38,39] A new flexibility in tailoring the topological surface states has been demonstrated. The effects of surface capping layers that tune the surface Fermi level and passivate the interface, or even the possibility of pinning the Fermi level near a Dirac point engineered to be well above the valence band, can now be explored and characterized.

Acknowledgements

The authors thank M. S. Fuhrer, Dohun Kim, T. D. Stanescu, and S. Das Sarma for helpful conversations, and A. Damascelli and Z.-H. Zhu for providing the ARPES data for the TSS dispersion of Bi_2Se_3. The UMD work is supported by DOE DE-SC0005436 and CNAM. The Rutgers work is supported by IAMDN, NSF DMR-0845464, and ONR N000140910749.

Appendix A: Models

Topological surface state dispersion

Peaks associated with the topological surface state in the momentum distribution curves as measured by ARPES[25,26] were fit along the Γ-K and Γ-M directions at many binding energies ranging from the valence band to well above the conduction band edge. Fits to the dispersion where energy is measured from the Dirac point give $E|_{\Gamma-K} = 1.7k + 13.5k^2 - 4,600k^6$ and $E|_{\Gamma-M} = 2.2k + 8.2k^2 + 4,200k^6$ where E_F is in eV and k is in $\mathring{A}^{-1}$. There is little difference between the two dispersions from hexagonal warping[40] since our range of Fermi level is from the Dirac point to just above the conduction band edge. The average of the two dispersions is used in the analysis and is given by $E_{avg} = 1.9k + 12.6k^2 + 2,300k^6$. The TSS Fermi velocity $v_F = dE/d(\hbar k)$, cyclotron mass $m_c = \hbar k_F / v_F$, and carrier density $n = k_F^2/(4\pi)$ are used in analyses.

Thomas-Fermi screening Model

Knowing the capacitance, a gate transfers a determined amount of net charge to or from a topological insulator. The net charge is distributed between the topological surface state and the bulk. Deriving this proportion requires solving the general band bending problem in a topological insulator due to screening of potentials.[41]

In the Thomas-Fermi screening model, the potential satisfies Poisson's equation which we solve for a semi-infinite slab of topological insulator subject to an externally applied electric field. Figure 5 shows band bending of the conduction band edge as a function of depth with a Fermi level E_{Fb} defined away from the screened region.

$$\frac{\partial^2 \phi(x)}{\partial x^2} = \frac{\rho(x)}{\epsilon}$$

The net electrostatic charge density is related to the net ionic background density n_0 and the carrier density of electrons n(x) by $\rho(x) = e(n_0 - n(x))$ where $n_0 = \frac{1}{3\pi^2}(2mE_{Fb}/\hbar^2)^{3/2}$ and $n(x) = \frac{1}{3\pi^2}(\frac{2m}{\hbar^2}(E_{Fb} - e\phi(x)))^{3/2}$

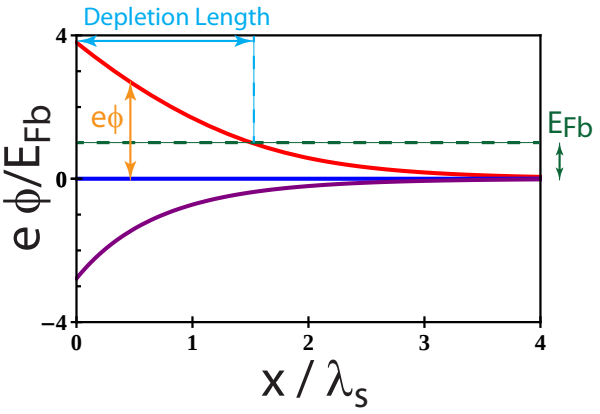

FIG. 5: Calculated band bending effects of the conduction band edge (red, blue, purple) in a semi-infinite slab of topological insulator. E_{Fb} (dashed green) is the Fermi level deep in the bulk, ϕ is the potential due to an externally applied electric field, λ_s is the screening length, and x is the distance away from the gated surface. Depletion onset occurs when $e\phi = E_{Fb}$. For larger ϕ (red), a depletion layer forms separating the topological surface state from the bulk carriers. Zero ϕ (blue) defines flat band where the background ion density equals the electron density. For negative ϕ (purple), the conduction band edge bends downward creating an accumulation layer.

The differential equation can be written in the following general form:

$$\frac{\partial^2 S}{\partial y^2} = (1-(1-S)^{3/2})$$

where $S = \frac{e\phi}{E_{Fb}}$, $y = \frac{x}{\lambda_s}$, and $\lambda_s^2 = \frac{\epsilon E_{Fb}}{e^2 n_0}$. λ_s defines the screening length and $\epsilon \approx 100$ for Bi_2Se_3.[22] Defining $E_S \equiv \frac{dS}{dy}$ and integrating, the second order differential equation is converted into a first order one. For the specific case of a semi-infinite slab where E_S and S are zero deep inside the topological insulator, the solution is simply given by:

$$E_S = \pm(2S + \frac{4}{5}(1-S)^{5/2} - \frac{4}{5})^{1/2}$$

Where the + (-) sign is for the case of band bending down (up), or equivalently $S(0) < 0$ ($S(0) > 0$). Depletion onset occurs when $S(0) = 1$. Either E_S or S on the inside surface at $y = 0$ is determined given an externally applied gate voltage and the uncompensated charge associated with the topological surface state whose dispersion is characterized by ARPES. From this solution, the carrier density associated with depletion for a surface Fermi level ΔE above flat band is found to be $n_d = n_0(\lambda_s^2 + \frac{2\epsilon}{n_0 e^2}\Delta E)^{1/2} - n_0\lambda_s$.

Optical Models

The optical models used to simulate the data are derived from a general solution to the transmission Fresnel coefficient for light normally incident on a stack of slabs which may have multiple conducting films at interfaces. The formalism is given in Reference 7, Appendix I.

Since the Parylene coating and In_2Se_3 capping layer are thin (compared to wavelength) non-absorbing dielectric films in our frequency range, they do not effect the optical signals so we omit them. The Bi_2Se_3 sample is a conducting film with optical absorptions due to phonons. Therefore the first boundary is between air and the Bi_2Se_3 slab, and between them is a NiCr film (used as a gate and characterized by the dc sheet resistance R_g). All contributions from all the free carriers in the Bi_2Se_3 film are lumped into $\sigma^{\pm}$. The second interface is between the Bi_2Se_3 and sapphire substrate. The last interface is sapphire into air with a NiCr film, an antireflection coating characterized by sheet resistance R_{AR}.

The Fresnel transmission coefficient $t^{\pm}$ are derived for the entire stack of slabs. All optical quantities presented in this paper are calculated from this expression.

The cyclotron resonance transmission is given by $T^+[V_g] = t^+\overline{t^+}$. The FTIR transmission spectra, although unpolarized, is given by the same expression with $B = 0$ and σ^+ replaced by the longitudinal polarization expression σ_{xx}.

For the differentially gated measurements, Δ-CR is given by

$$\frac{\Delta T^+}{T_{avg}} = \frac{T^+[V_g + \Delta V/2] - T^+[V_g - \Delta V/2]}{\frac{1}{2}(T^+[V_g + \Delta V/2] + T^+[V_g - \Delta V/2])}$$

Unpolarized gated FTIR measurements are reported normalized to the zero gate transmittance and is given by (where B is set to zero)$\frac{T^+[V_g]}{T^+[V_g=0]}$. $\Delta\theta_F$ is given by $\Delta\theta_F[V_g] = \theta_F[V_g + \Delta V/2] - \theta_F[V_g - \Delta V/2]$.

There are two prominent phonons in Bi_2Se_3 over our spectral range of interest which can be written in terms of the complex index of refraction $n_{BiSe} = \sqrt{\epsilon}$ where $\epsilon = \epsilon_0 + \sum_{i=1}^{2}\epsilon_i$ and $\epsilon_i = \frac{\Omega_i^2}{\omega_i^2 - \omega^2 - i\omega\Gamma_i}$. The phonon parameters for epitaxial films are experimentally determined to be $\epsilon_0 = 25.6$, $\Omega_1 = 615\ \mathrm{cm}^{-1}$, $\omega_1 = 63.1\ \mathrm{cm}^{-1}$, $\Gamma_1 = 1.8\ \mathrm{cm}^{-1}$, $\Omega_2 = 80\ \mathrm{cm}^{-1}$, $\omega_2 = 133\ \mathrm{cm}^{-1}$, and $\Gamma_2 = 2\ \mathrm{cm}^{-1}$. Similar values for bulk crystals were previously reported.[22]

The free carrier response of the Bi_2Se_3 film is modeled as the sum of three Drude terms $\sigma^{\pm} = \sum_{i=1}^{3}\frac{\omega_{ps,i}/Z_0}{\gamma_i - i(\omega_i \pm \omega_{c,i})}$ where $\omega_{c,i} = eB/cm_{c,i}$ is the cyclotron frequency, $\omega_{ps,i} = Z_0 n_i e^2/m_{c,i}$ is the two dimensional plasma frequency, γ_i is the inverse transport lifetime, $m_{c,i}$ is the cyclotron mass, n_i is the two dimensional carrier density, and Z_0 is the impedance of free space.

NiCr films are used as a gate and antireflection (AR) coating since NiCr has a very high scattering rate. Therefore, the admittance is frequency independent at THz frequencies. The optical response is then completely characterized by the dc sheet resistance where $R_{AR} = 275\ \Omega$,

and $R_g = 400\ \Omega$. Other parameters are the index of refraction of sapphire $n_{Saph} = 3.1$ and vacuum $n_0 = 1$, the thickness of the sapphire substrate $d_{Saph} = .05$ cm, and the Bi_2Se_3 film thickness $d_{BiSe} = 60$ nm.

Appendix B: More gate-modulated optical data

Figures 6(a) and (b) report Δ-CR data that are similar to Figure 2(a) except the measurements were performed at different frequencies. Differential Fourier transform spectroscopy data (Δ-FTIR) is reported in Figure 6(c). Figures 6(d-f) are the corresponding modeled optical responses that use the same parameters as reported in Figure 3.

The oscillations present in the FTIR data are from Fabry-Perot interference occurring in the substrate due to an imperfect antireflection coating. The increase in transmission with negative gate voltage is evidence of dominant n-type carriers. If a single Drude n-type carrier existed and a gate changed only the carrier density, then the data set would be fully symmetric about zero gate bias. The asymmetry is an indication of a gate-dependent scattering rate and/or mass.

In the case of the model in Figures 6(f), the main effect is produced by the gate-dependent MTB carrier scattering rate with some effects from the TSS carriers. For increasing positive gate voltages, the MTB and TSS carriers have progressively larger masses and scattering rates giving rise to progressively smaller changes in conductivity. For negative gate voltages, the opposite is true so the changes in conductivity are larger.

A 7 mm spot size was used for the FTIR measurements. Such a large spot size relative to the sample allows the maximum of throughput power required to measure to low frequencies. However, some leakage light occurred through ungated parts of the film due to the shadow masking procedure. The measured Δ-FTIR signals are therefore reduced. Although the photometrics noticeably deviate from the model, the qualitative behavior is reproduced. As described in the main text, the omission of potential fluctuation effects at high negative gate voltages cause the model to overestimate the gated optical response. The apparent asymmetric response observed in the transmission associated with the phonon resonance in Figures 1(c) and 6(c) is reproduced by a simple Lorentzian dielectric response function and follows from the divergence of the real part of ϵ associated with the transverse-optical phonon at $f \approx 1.9$ THz.

Appendix C: Extended Discussion

Carrier distributions, potential fluctuations, and conduction band edge location

The bulk carrier density is measured to be $\lesssim 5 \times 10^{17}$ cm^{-3} by dc characterization of films as a function of film thickness.[10] The cyclotron mass is $\sim 0.2\ m_0$ (taken directly from the terahertz Faraday and cyclotron resonance data of Figure 1). The screening length λ_s depends weakly on bulk density, so it is ~ 11 nm. The bulk density corresponds to a bulk Fermi level of ~ 11 meV.

Using the entire analysis with a three-fluid fit to the zero-gate data that incorporates results from the differential measurements, the total carrier density at zero gate is 1.44×10^{13} cm^{-2} distributed between the BSAL contribution of 1.0×10^{13} cm^{-2} and the top surface contribution of 4.4×10^{12} cm^{-2}.

The gated optical measurements, independent of the dc characterization, show that most of the charge measured at zero gate resides in the bottom section of the film. As described in the main text, the very small measured mass at large negative gate voltage in the Δ-CR data indicates the top surface state has a Fermi level very close to the Dirac point at -170 V. Only 1.7×10^{12} cm^{-2} excess carriers exist on the top surface at zero gate. The remaining $> 10^{13}$ cm^{-2} carriers measured at zero gate are in the bottom surface and bulk. This result presumes the conduction band edge is at 190 meV above the Dirac point as measured by ARPES.

For the shifted Dirac cone deduced from the step in scattering rate, one of the main findings of the paper, the top surface carrier density at zero gate is somewhat larger than previously estimated. Before it is possible to estimate the net carrier density n_s on the top surface at zero gate, it is necessary to first determine the surface Fermi level of the conduction band edge located at -70 V (while the Dirac point remains at -170 V)

For the case of this shifted Dirac cone, gating from the Dirac point (-170 V) to the conduction band edge (-70 V) transfers $n_g = 2.6 \times 10^{12}$ cm^{-2} carriers that fill the surface state up to the conduction band edge with n_{tss} carriers as well as fill the depletion layer with n_d carriers. n_{tss} is found from the ARPES dispersion and the Fermi level of the conduction band edge, E_c. Solving $n_g = n_d(E_c) + n_{tss}(E_c)$ gives $E_c = 80$ meV where $n_{tss} = 1 \times 10^{12}$ cm^{-2} and $n_d = 1.6 \times 10^{12}$ cm^{-2}. The excess charge on the surface at zero gate is $n_s = 2.8 \times 10^{12}$ cm^{-2}. Again we can conclude that the large majority of the carriers reside on the bottom surface of the film at zero gate.

By solving the full Thomas-Fermi screening model with the conduction band edge set at 80 meV above the Dirac point, the surface Fermi level E_F as a function of gate voltage can be calculated, similar to Figure 3(b). Such a treatment provides estimates of the potential fluctuation energies. As specified in the main text, the onset of potential fluctuations near the Dirac point occurs at -130 V. This voltage corresponds to a surface Fermi level of 50 meV. Taking a derivative of the scattering rate curve shown in Figure 3(d) shows a gaussian-like structure centered on the step at -70 V where the FWHM points are at -100 V and -40 V, corresponding to an energy width of 50 meV. The 1/2-width is compared with the Dirac point potential fluctuation onset energy in the main text.

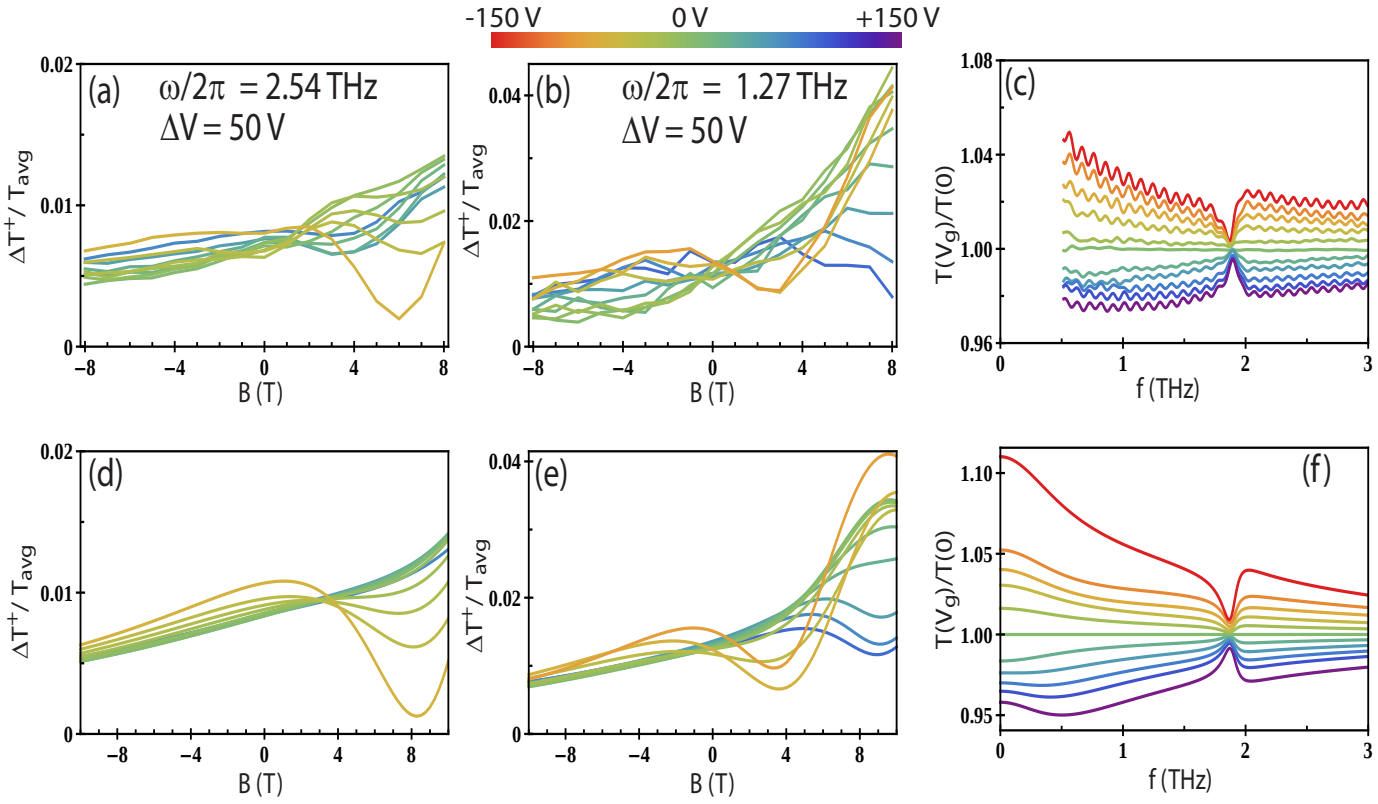

FIG. 6: **Gated optical transmission measurements addenda** (a-b) 10K Δ-CR measurements are the same as described in the caption of Figure 2 except measured at different frequencies labeled on each graph (c) 6 K zero magnetic field FTIR transmission measured at gate voltage V_g normalized to the zero gate value. (d-f) the corresponding modeled optical responses using the same parameters reported in Figure 3 that reproduce the data of Figures 2(a-c) and Figures 1(c,d).

Using the dc characterized bulk density is not necessary to conlucde that most carriers in the film reside on the bottom. larger assumed bulk densities n_0 imply larger n_d, and therefore fewer carriers on the top surface at zero gate.

For a bulk density of 5×10^{17} cm^{-3}, whether the conduction band edge is at 80 or 190 meV, the depletion region extends across at least half of the film at $V_g = -170$ V. For larger bulk densities, the depletion length becomes smaller. The BSAL Drude conductivity contribution can involve the bottom surface accumulation layer and any bulk contribution not depleted at $V_g = -170$ V.

It is not *a priori* obvious that three Drude terms should suffice in the model since numerous other conductivity contributions could be associated with bulk and accumulated carriers. For the bottom surface accumulation layer (BSAL), there may exist subband states associated with the bulk accumulation, and the lowest subbands may be Rashba split.[25,36] However, multiple bottom surface carrier contributions are not discernable in the zero-gate measurements nor the differential optical measurements that are not very sensitive to the details of the BSAL.

The three-term Drude model impressively reproduces the features of all the data sets with only three free parameters allowing clean extraction of the TSS parameters.

Cyclotron and SdH mass

The measured cyclotron mass of the bulk MTB carriers (0.21) near the conduction band edge as well as the BSAL mass (0.25) may at first appear large. The Shubnikov-de Haas (SdH) measured mass in bulk crystals is $0.13-0.15$ near the conduction band edge with a carrier density of $\sim 10^{17}$ cm^{-3}, and shows no discernible non-parabolicity up to $\sim 5 \times 10^{19}$ cm^{-3}.[24,42–46] This behavior of the SdH mass may seem peculiar considering that, as is generally known, the band dispersion in small-gap semiconductors is ordinarily non-parabolic causing the band mass, and therefore the cyclotron mass, to increase with surface Fermi energy.

For systems with degenerate carriers, however, many-body interactions can complicate direct comparison of measured masses.[47] In SdH (and ARPES) the measured cyclotron frequency differs from the band value

due to self-energy corrections coming from the electron-electron interaction due to the Coulomb interaction and the Frohlich interaction due to the polar phonon.

This effect is dependent on carrier density and may differ for 2D and 3D electron systems. In the case of cyclotron resonance, final state interactions associated with the photo-generated electron-hole pair (exciton effect) can lead to a shift of the cyclotron resonance frequency compared with the SdH (or deduced from ARPES). This excitonic shift tends to compensate for the self-energy effects resulting in a cyclotron resonance that tends to be closer to the bare-band value. The Kohn thereom[48–50] shows that this compensation is exact for pure Coulomb interactions in an isotropic 2D electron liquid or a 3D electron liquid at q=0.

Unfortunately, there has not been much work comparing SdH and magneto-optical data to sort out these many-body effects in Bi_2Se_3 or related materials. In our earlier work,[7,22] the bulk magneto-transmission yielded a band edge mass of 0.15. However, in this measurement which is dominated by magneto-plasma effects, $q \neq 0$ so that the cyclotron mass should be compared with the SdH mass with which it agrees.

Measurements on PbTe and bismuth metal illustrate these many-body interaction effects.[48–50] We note that r_s, the ratio of the electronic potential to kinetic energy and a general measure of the strength of interactions, is larger for Bi_2Se_3 ($r_s = 0.2$) compared with bismuth ($r_s = 0.1$) so that larger exciton shifts are expected.

In view of these considerations the observation of a $\sim$ 0.2 mass for the MTB channel is not surprising. In these thin films, $q = 0$ and so final state interactions effects are relevant. In addition, the mass observed for the zero-gate optical response of Figure 1, which is dominated by the BSAL, appears to be even larger in our work as well as the work of Armitage *et al.*[23]

These cyclotron mass issues deserve further study in these topologically interesting materials.

* URL: http://www.irhall.umd.edu; Electronic address: GregJenkins@MyFastMail.com

[1] M. Z. Hasan and C. L. Kane, Reviews of Modern Physics **82**, 3045 (2010).
[2] X.-L. Qi and S.-C. Zhang, Reviews of Modern Physics **83**, 1057 (2011).
[3] J. Maciejko, X.-L. Qi, H. D. Drew, and S.-C. Zhang, Physical Review Letters **105**, 166803 (2010).
[4] X.-L. Qi, T. L. Hughes, and S.-C. Zhang, Physical Review B **78**, 195424 (2008).
[5] Y. Xia, D. Qian, D. Hsieh, L. Wray, A. Pal, H. Lin, A. Bansil, D. Grauer, Y. S. Hor, R. J. Cava, et al., Nature Physics **5**, 398 (2009).
[6] N. P. Butch, K. Kirshenbaum, P. Syers, A. B. Sushkov, G. S. Jenkins, H. D. Drew, and J. Paglione, Physical Review B **81**, 241301 (2010).
[7] G. S. Jenkins, A. B. Sushkov, D. C. Schmadel, N. P. Butch, P. Syers, J. Paglione, and H. D. Drew, Physical Review B **82**, 125120 (2010).
[8] J. G. Analytis, R. D. McDonald, S. C. Riggs, J.-H. Chu, G. S. Boebinger, and I. R. Fisher, Nature Physics **6**, 960 (2010).
[9] H. Steinberg, D. R. Gardner, Y. S. Lee, and P. Jarillo-Herrero, Nano Letters **10**, 5032 (2010).
[10] N. Bansal, Y. S. Kim, M. Brahlek, E. Edrey, and S. Oh, Physical Review Letters **109**, 116804 (2012).
[11] D. Kong, J. J. Cha, K. Lai, H. Peng, J. G. Analytis, S. Meister, Y. Chen, H.-J. Zhang, I. R. Fisher, Z.-X. Shen, et al., ACS Nano **5**, 4698 (2011).
[12] J. G. Checkelsky, Y. S. Hor, R. J. Cava, and N. P. Ong, Physical Review Letters **106**, 196801 (2011).
[13] V. Korenman and H. D. Drew, Physical Review B **35**, 6446 (1987).
[14] D. Agassi and V. Korenman, Physical Review B **37**, 10095 (1988).
[15] P. Roushan, J. Seo, C. V. Parker, Y. S. Hor, D. Hsieh, D. Qian, A. Richardella, M. Z. Hasan, R. J. Cava, and A. Yazdani, Nature **460**, 1106 (2009).
[16] H. Beidenkopf, P. Roushan, J. Seo, L. Gorman, I. Drozdov, Y. S. Hor, R. J. Cava, and A. Yazdani, Nature Physics **7**, 939 (2011).
[17] N. Bansal, Y. S. Kim, E. Edrey, M. Brahlek, Y. Horibe, K. Iida, M. Tanimura, G.-H. Li, T. Feng, H.-D. Lee, et al., Thin Solid Films **520**, 224 (2011).
[18] M. Brahlek, N. Bansal, N. Koirala, S.-Y. Xu, M. Neupane, C. Liu, M. Z. Hasan, and S. Oh, Physical Review Letters **109**, 186403 (2012), URL http://link.aps.org/doi/10.1103/PhysRevLett.109.186403.
[19] D. Kim, S. Cho, N. P. Butch, P. Syers, K. Kirshenbaum, S. Adam, J. Paglione, and M. S. Fuhrer, Nature Physics **8**, 460 (2012).
[20] A. Kahouli, A. Sylvestre, L. Ortega, F. Jomni, B. Yangui, M. Maillard, B. Berge, J. C. Robert, and J. Legrand, Applied Physics Letters **94**, 152901 (2009).
[21] G. S. Jenkins, D. C. Schmadel, and H. D. Drew, Review of Scientific Instruments **81**, 083903 (2010).
[22] A. B. Sushkov, G. S. Jenkins, D. C. Schmadel, N. P. Butch, J. Paglione, and H. D. Drew, Physical Review B **82**, 125110 (2010).
[23] R. Valdes Aguilar, A. V. Stier, W. Liu, L. S. Bilbro, D. K. George, N. Bansal, L. Wu, J. Cerne, A. G. Markelz, S. Oh, et al., Physical Review Letters **108**, 087403 (2012).
[24] H. Kohler, physica status solidi (b) **58**, 91100 (1973).
[25] Z.-H. Zhu, G. Levy, B. Ludbrook, C. N. Veenstra, J. A. Rosen, R. Comin, D. Wong, P. Dosanjh, A. Ubaldini, P. Syers, et al., Physical Review Letters **107**, 186405 (2011).
[26] Z. Zhu and A. Damascelli (2012), private communication.
[27] S. M. Sze, *Physics of Semiconductor Devices, 2nd Edition* (John Wiley & Sons, 1981), ISBN 9780471056614.
[28] S. Das Sarma, S. Adam, E. H. Hwang, and E. Rossi, Reviews of Modern Physics **83**, 407 (2011).
[29] J.-H. Chen, C. Jang, S. Adam, M. S. Fuhrer, E. D. Williams, and M. Ishigami, Nature Physics **4**, 377 (2008).
[30] J. Horng, C.-F. Chen, B. Geng, C. Girit, Y. Zhang, Z. Hao, H. A. Bechtel, M. Martin, A. Zettl, M. F. Crommie, et al., Physical Review B **83**, 165113 (2011).
[31] Y.-C. Ruan and W. Y. Ching, Journal of Applied Physics

62, 2885 (1987).
[32] S. Drapak, Z. Kovalyuk, V. Netyaga, and V. Orletskii, Technical Physics Letters **28**, 707 (2002).
[33] S. Sakalauskas and A. Sodeika, Review of Scientific Instruments **69**, 466 (1998).
[34] M. H. Berntsen, O. Gotberg, and O. Tjernberg, arXiv:1206.4183 (2012).
[35] D. Culcer, E. H. Hwang, T. D. Stanescu, and S. Das Sarma, Physical Review B **82**, 155457 (2010).
[36] M. Bianchi, D. Guan, S. Bao, J. Mi, B. B. Iversen, P. D. C. King, and P. Hofmann, Nature Communications **1**, 128 (2010).
[37] Y. L. Chen, J. G. Analytis, J. H. Chu, Z. K. Liu, S. K. Mo, X. L. Qi, H. J. Zhang, D. H. Lu, X. Dai, Z. Fang, et al., 0904.1829 (2009), URL `http://arxiv.org/abs/0904.1829`.
[38] T. Hanaguri, K. Igarashi, M. Kawamura, H. Takagi, and T. Sasagawa, Physical Review B **82**, 081305 (2010).
[39] P. Cheng, C. Song, T. Zhang, Y. Zhang, Y. Wang, J.-F. Jia, J. Wang, Y. Wang, B.-F. Zhu, X. Chen, et al., Physical Review Letters **105**, 076801 (2010).
[40] L. Fu, Physical Review Letters **103**, 266801 (2009).
[41] D. Galanakis and T. D. Stanescu, arXiv:1206.2043 (2012).
[42] J. G. Analytis, J.-H. Chu, Y. Chen, F. Corredor, R. D. McDonald, Z. X. Shen, and I. R. Fisher, Physical Review B **81**, 205407 (2010).
[43] K. Eto, Z. Ren, A. A. Taskin, K. Segawa, and Y. Ando, Physical Review B **81**, 195309 (2010).
[44] V. A. Kulbachinskii, N. Miura, H. Nakagawa, H. Arimoto, T. Ikaida, P. Lostak, and C. Drasar, Physical Review B **59**, 1573315739 (1999).
[45] G. Hyde, R. Dillon, H. Beale, I. Spain, J. Woollam, and D. J. Sellmyer, Solid State Communications **13**, 257263 (1973).
[46] J. Navratil, J. Hork, T. Plechacek, S. Kamba, P. Lostak, J. Dyck, W. Chen, and C. Uher, Journal of Solid State Chemistry **177**, 17041712 (2004).
[47] P. M. Platzman and P. A. Wolff, *Waves and interactions in solid state plasmas* (Academic Press, 1973), ISBN 9780126077735.
[48] S. W. McKnight and H. D. Drew, Physical Review B **21**, 34473466 (1980).
[49] H. R. Verdun, Physical Review Letters **33**, 16081611 (1974).
[50] H. R. Verdun and H. D. Drew, Physical Review B **14**, 13701394 (1976).